Mine Water Environ (2017) 36:463–478
DOI 10.1007/s10230-017-0452-6

TECHNICAL ARTICLE

Exploration of Diffuse and Discrete Sources of Acid Mine Drainage to a Headwater Mountain Stream in Colorado, USA

Allison Johnston[1] · Robert L. Runkel[2] · Alexis Navarre-Sitchler[1,3] · Kamini Singha[1,3]

Received: 28 June 2016 / Accepted: 18 April 2017 / Published online: 29 April 2017

Abstract We investigated the impact of acid mine drainage (AMD) contamination from the Minnesota Mine, an inactive gold and silver mine, on Lion Creek, a headwater mountain stream near Empire, Colorado. The objective was to map the sources of AMD contamination, including discrete sources visible at the surface and diffuse inputs that were not readily apparent. This was achieved using geochemical sampling, in-stream and in-seep fluid electrical conductivity (EC) logging, and electrical resistivity imaging (ERI) of the subsurface. The low pH of the AMD-impacted water correlated to high fluid EC values that served as a target for the ERI. From ERI, we identified two likely sources of diffuse contamination entering the stream: (1) the subsurface extent of two seepage faces visible on the surface, and (2) rainfall runoff washing salts deposited on the streambank and in a tailings pile on the east bank of Lion Creek. Additionally, rainfall leaching through the tailings pile is a potential diffuse source of contamination if the subsurface beneath the tailings pile is hydraulically connected with the stream. In-stream fluid EC was lowest when stream discharge was highest in early summer and then increased throughout the summer as stream discharge decreased, indicating that the concentration of dissolved solids in the stream is largely controlled by mixing of groundwater and snowmelt. Total dissolved solids (TDS) load is greatest in early summer and displays a large diel signal. Identification of diffuse sources and variability in TDS load through time should allow for more targeted remediation options.

Keywords Characterization · Electrical resistivity · Fluid conductivity

✉ Allison Johnston
a.johnston0@gmail.com

[1] Hydrologic Science and Engineering Program, Colorado School of Mines, 1516 Illinois Street, Golden, CO, USA

[2] US Geological Survey Toxic Substances Hydrology Program, 3215 Marine Street, Boulder, CO, USA

[3] Geology and Geological Engineering Department, Colorado School of Mines, 1516 Illinois Street, Golden, CO, USA

Introduction

There are thousands of inactive mines in the Colorado Mineral Belt, a legacy of the gold and silver rushes in the state's history (Lovering and Goddard 1950). Many of the mines have not been active for nearly a century, are poorly documented, and no longer have a clear owner or responsible party. These mines are an environmental concern as water drains through mine adits and tailings piles, weathering the partially mined ore (e.g. Banks et al. 1997; Chandra and Gerson 2010). Metal sulfide minerals release proton acidity as they weather (e.g. Chandra and Gerson 2010; Evangelou and Zhang 1995; Johnson and Hallberg 2005; Moses and Herman 1991; Nordstrom 2011), and are the main cause of acid mine drainage (AMD). Pyrite is the most abundant sulfide mineral in the Earth's crust and is often found with valuable minerals such as gold, silver, copper, and uranium (e.g. Evangelou and Zhang 1995). Pyrite oxidation is the biggest contributor of acidity and dissolved iron to AMD (e.g. Banks et al. 1997; Johnson and Hallberg 2005; Nordstrom 2011).

In most mine environments, pyrite oxidation by ferric iron is much faster than oxidation by dissolved oxygen (Moses et al. 1987; Taylor et al. 1984) due to more favorable reaction kinetics (Luther 1987) and the microbially-mediated oxidation of ferrous iron that resupplies

ferric iron (e.g. Evangelou and Zhang 1995). Although the mechanism and kinetics of pyrite oxidation are not fully understood, it is generally accepted that the reaction occurs on the surface of the pyrite, which explains why mining enhances pyrite weathering by increasing the surface area of pyrite or other metal sulfides exposed to oxygenated water. The combination of low pH, high metal concentrations, and metal oxides deposited on the streambed in AMD-impacted systems results in high stress on the lotic ecosystem, leading to reductions of macroinvertebrate abundance and diversity as well as changes in composition of the algal community (DeNicola and Stapleton 2002; Niyogi et al. 2002). The US Bureau of Mines estimated that AMD has adversely affected 6500 km of streams and rivers in the US (Kleinmann 1991).

A challenge in these complex flow environments is the characterization of seasonal variation in the load and sources of AMD constituents. Stream hydrographs in the Rocky Mountains are generally snow dominated, with as much as 80% of annual precipitation occurring as snow (Baron and Campbell 1997; Brooks et al. 2001). Seasonal variation in stream discharge drives much of the variation in stream chemistry in snow-dominated systems (e.g. Boyer et al. 1997). Snowmelt sometimes drives a spike in the concentration of AMD constituents at the beginning of spring runoff, known as 'first flush' (e.g. Boyer et al. 1997; Brooks et al. 2001; Hornberger et al. 1994; Nordstrom 2009, 2011). Hornberger et al. (1994) and Boyer et al. (1997) describe the first flush mechanistically as the result of water table rise during spring melt, which flushes out chemical species that built up in pore water during low flow conditions. This leads to high concentrations during the rising limb of the stream hydrograph when the water table first rises during spring snowmelt, followed by declining concentrations during the falling limb of the stream hydrograph because the chemical species that accumulated during low flow have already been flushed out (Boyer et al. 1997; Brooks et al. 2001; Byrne et al. 2013).

The extent of first flush behavior on AMD constituents varies between different mining-impacted snow-dominated systems. Two studies illustrating different seasonal concentration regimes are highlighted here as a demonstration, although there are many more (e.g. Byrne et al. 2013). For example, Kimball et al. (2010) found that the concentrations of iron, manganese, and zinc in the Animas River in southwestern Colorado were similar throughout the year; thus, metal loading (mass of metals passing through the stream per time) was highest when flow was highest. However, calcium and magnesium concentrations were diluted during high flows, resulting in an increased hardness-based toxicity during high flows even though concentrations were lower. Sullivan and Drever (2001) found that metal concentrations in drainage directly from Pennsylvania Mine, near Keystone, Colorado, were highest during maximum snowmelt and declined over the summer. This illustrates first flush behavior. However, Peru Creek, a stream impacted by flow from that mine, displayed the opposite behavior. Dissolved metal concentrations in Peru Creek were lowest during maximum snowmelt and increased over the summer, although again metal loads were highest during high flows. The authors suggest that this is due to changing proportions of dilute snowmelt and AMD in the stream throughout the summer. Consequently, while the metal load of common AMD constituents is often higher during high flow, site-specific factors cause temporal variations in concentration, sources of major AMD constituents, and hardness levels, the last of which can affect the toxicity of metal contaminants. In addition, metal concentrations are often at their highest levels during low-flow periods when sources of contamination are undiluted by snowmelt and/or rainfall; low flow is thus a critical time period for aquatic toxicity (Besser and Leib 1999; Grayson et al. 1997). Further, seasonal and diel variations in metal concentrations are sometimes so great that a site exceeds regulatory standards for only part of a day or year (e.g. Kimball et al. 2006, 2010; Nimick et al. 2011; Nordstrom 2011).

Effective remediation of these sites requires extensive site characterization, including detailed spatial information about AMD sources, which may be discrete or diffuse. Baresel et al. (2006) constructed a watershed-scale cost-minimization model for a river in Sweden affected by AMD and found that the spatial distribution of the point and diffuse AMD sources was critical for spatially targeted, cost-effective remediation measures. While discrete sources are typically easy to identify, diffuse sources are more difficult to detect and can contribute a significant contaminant load (e.g., Banks and Palumbo-Roe 2010). Diffuse sources include contaminated groundwater entering the stream in gaining reaches, entrainment of metal-rich sediment, redissolution of metals that had previously precipitated, and storm runoff routed through tailings piles (Gozzard et al. 2011; Nordstrom 2011). Several studies have found that the relative contribution of AMD constituents from point and diffuse sources varies seasonally. For example, during low flows, Gozzard et al. (2011) found that over 60% of the total zinc in the River West Allen watershed in the UK was from one of three point sources. During high flows, only 7% of the total zinc was from point sources. Likewise, Kimball et al. (2010) found that the contribution of point sources was much greater during low flows than high flows. The results from these studies and others (e.g. Runkel et al. 2016; Walton-Day et al. 2012) emphasize the importance of diffuse sources of contamination as well as seasonal variation in contamination sources. Quantifying the load from all sources is important for helping remediation decision makers to identify critical times of the year when metal

loading is high, estimate cumulative amounts of contaminants, and plan maintenance activities accordingly.

Hydrologic tracer techniques (e.g. Bencala and Walters 1983) combined with synoptic sampling are commonly used methods of AMD site characterization. These techniques provide a detailed spatial profile of discharge and AMD contaminant concentration through the study reach. This information is used to determine incremental and cumulative metal loading along the study reach, to identify sources, and to constrain development of reactive transport models (Butler et al. 2009; Caruso et al. 2008; Kimball et al. 2002; Runkel et al. 2012, 2013). However, there are limited methods for investigating diffuse contamination in AMD-impacted streams. Incremental metal loading profiles can indicate which segments of the stream are affected by diffuse contamination during the flow regime in which the study takes place. However, it can be costly to obtain the temporal and spatial resolution needed to accurately characterize diffuse sources using these techniques.

Geophysical methods also have been used to identify areas of diffuse contamination. Electrical resistivity imaging (ERI), in particular, is frequently used in applications where the contaminants of interest result in an increase in fluid electrical conductivity (EC). Elevated fluid EC increases bulk EC, which is measured by ERI. ERI has been used to map bulk EC for AMD site characterization in numerous studies. Ebraheem et al. (1990), for example, measured bulk EC associated with highly contaminated mine water to identify three valleys in which mine spoil was deposited during mining operations. Rucker et al. (2009a, b) used ERI to identify the most contaminated areas at an abandoned mine site, and noted a fracture zone that potentially transported AMD-impacted water from mine spoils to a perennial stream. Martìn-Crespo et al. (2011) used ERI to examine the geometry of mine ponds, looking for infill thickness and leaks, and supplemented this work with mineralogical and geochemical data describing the composition of mine ponds so that they could estimate potential pollution in the event of a release. Bethune et al. (2015) used time-lapse ERI to look at seasonal change in mine-impacted water flow from an inactive mine to a headwater mountain stream. The studies described above, and others (e.g. Buselli and Lu 2001; Ramalho et al. 2009) have demonstrated the utility of ERI as a non-invasive, cost-effective site-investigation technique for AMD-impacted sites.

Here, we applied ERI to the characterization of a mining-impacted stream in Colorado to identify diffuse sources of AMD in addition to readily identified discrete sources. The study location is Lion Creek, a small headwater stream in the Empire Mining District, approximately 60 km west of Denver, Colorado. The study area has a long history of gold and silver mining dating back to the late 1800s (Lovering and Goddard 1950), and acidic drainage from the nearby Minnesota Mine is a potential source of contamination to Lion Creek. We used ERI, fluid EC in the stream, and geochemical analysis of surface water samples to compare relative amounts of AMD entering the stream from June to October, from snowmelt to the late-summer drying-out period. Our objectives were threefold: (1) to identify diffuse and discrete contamination sources, (2) to elucidate seasonal trends in water quality and loading, and (3) to help inform ongoing remediation efforts.

Field Site

The Minnesota Mine and Mill is a historic gold mine located 2 km northwest of the town of Empire, Colorado, in Clear Creek County (Fig. 1). The gold ore found in Minnesota Mine is almost all the pyritic gold type, making it likely to produce AMD (Cunningham et al. 1994; Lovering and Goddard 1950). The veins of the mine are in the Precambrian Boulder Creek Granite on the northwest side of a 300-m wide diameter stock of monzonite porphyry (Braddock 1969; Cunningham et al. 1994; Lovering and Goddard 1950). The Minnesota Mine includes 2100 m of underground workings on numerous levels. The upper levels of the mine access the Atlantic and Comet veins and are drained by a main portal that is adjacent to a shaft that accessed the lower levels (Lovering and Goddard 1950). At the time of this study, the main portal was collapsed and water exiting the collapsed adit flowed along a short channel before entering a grated concrete chamber that has been placed over the shaft collar. Water levels in the shaft (elevation 2963 m) were 0–2 m below the top of the shaft over the course of this study, indicating that the lower mine levels were completely flooded.

Minnesota Mine and the immediately adjacent section of Lion Creek are part of the Clear Creek/Central City Superfund Site. In 1995, the US Forest Service (USFS) entered into a cooperative agreement with the US Environmental Protection Agency (EPA) to clean up 28,000 m^2 of USFS property (Dodson 2004). The chief concern was sediment loading from the tailings pile (most of the area encompassed by the 1996 remediation area in Fig. 1) entering Lion Creek after storm events, as well as cadmium, copper, zinc, iron, and manganese concentrations exceeding State of Colorado water quality standards (Looby 1991). Clear Creek is a drinking water source for a quarter of a million people in the Denver area and a major recreation area, so water quality is a major concern (Sims and Guerra 2014). The area directly below the mine outlet was graded, capped, and seeded for erosion control in November 1996, although the tailings were not removed (Dodson 2004). The erosion-control measures have ameliorated the problem of sediment entering Lion Creek and being

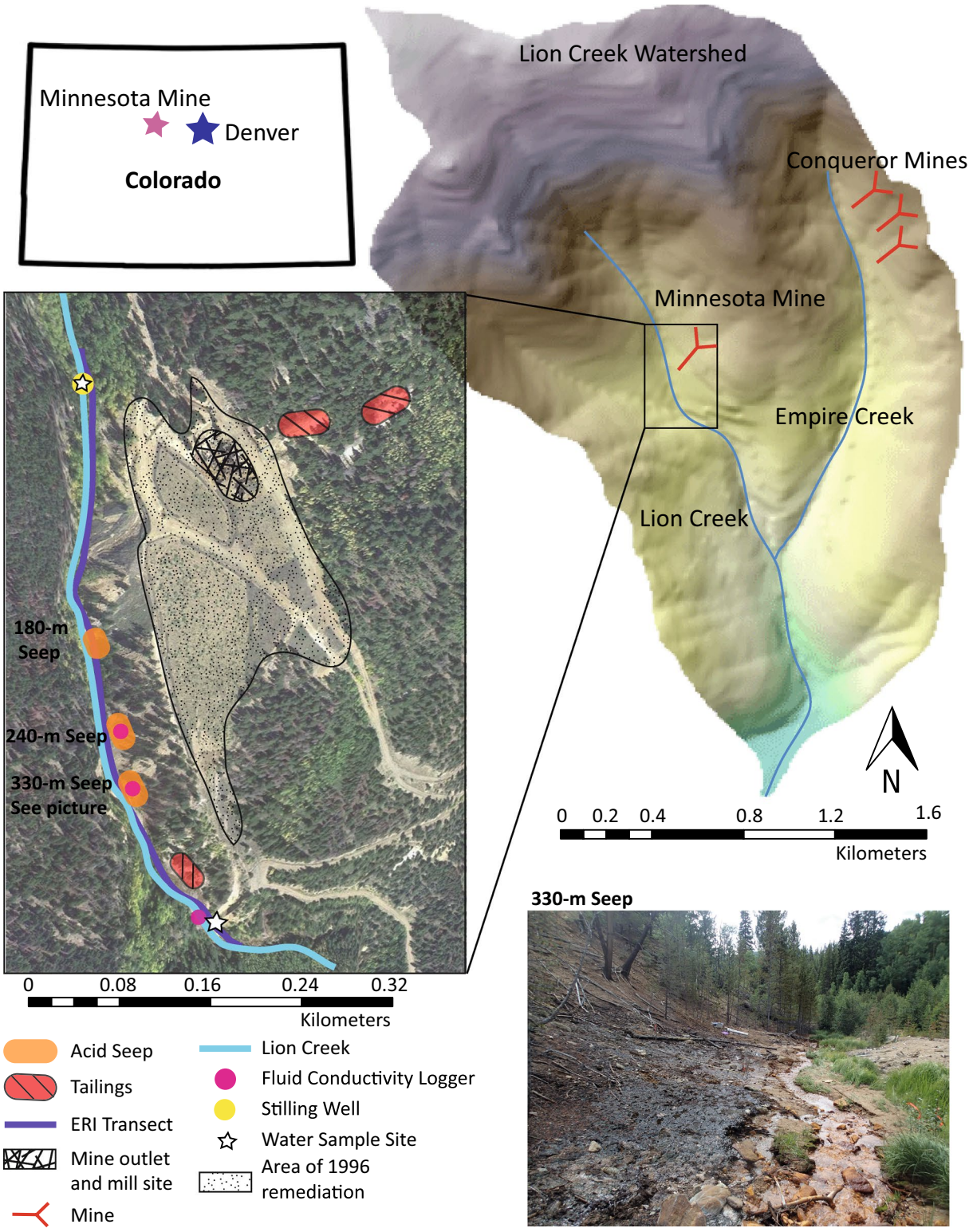

Fig. 1 Overview of field site and instrumentation locations. The upstream sample location is from Upper Lion Creek and the downstream sample location is from Lower Lion Creek. Aerial photograph from Google Maps© 2016, imagery date 9 Oct. 2015. The Lion Creek Watershed cutout is colored by elevation. The photograph in the *lower right* shows the view to the south of the 330-m seep. Note the streambed coated with iron oxide precipitates that form when low-pH, metal-rich stream water mixes with higher pH stream water

carried downstream; however, Lion Creek still appears to be impacted by Minnesota Mine as evidenced by tailings on the east bank of Lion Creek and orange and white precipitate coating large areas of the streambed. The USFS is, as of December 2016, planning additional remedial actions that will directly address water quality in Lion Creek (T. Skillern, USFS; personal communication 19 April 2016).

Downgradient from the mine outlet there are three major areas where water seeps out of the steep east streambank and enters Lion Creek (Fig. 1). The seeps in this study are described by their position along Lion Creek, with 0 being the farthest upstream point investigated, at an elevation of 2961 m (distances used herein are from a companion study conducted in August 2014; see Byrne et al. 2017). The first seepage area, the '180-m seep', extends from 176 to 182 m and has an average pH of 3.2. The '240-m seep' emanates from a large eroded area, where water having an average pH of 2.6 seeps out of the steep streambank from 238 to 270 m. The '330-m seep', located from 324 to 342 m, has an average pH of 2.4. In this area, a large seepage face is present (Fig. 1, photograph). The presence of the seepage face and low pH of the seepage water indicates possible hydrogeologic connections between the mine pool contained in the Minnesota Mine workings (also indicated by the water level observed in the shaft) and Lion Creek. However, this could also be due to weathering of mineralized veins unrelated to mining, or from the tailings remaining in the reclaimed field. Orange iron precipitate coats the streambed beginning upstream from the acidic seeps, indicating that contamination entering Lion Creek is not restricted to the visible seepage areas, but is also potentially caused by diffuse sources.

Methods

This study used three methods to characterize the impacts of AMD on Lion Creek: geochemical analyses (i.e. water quality sampling and load calculations), fluid EC logging in the stream and the seeps, and ERI. Water samples were collected to monitor the concentration of dissolved metals (operationally defined as the fraction that passes through a 0.45 μm filter) in the stream to help interpret the EC measurements. Fluid EC logging, using EC transducers, was used to observe diel, seasonal, and event-based changes in stream and seep fluid EC in a more continuous fashion than could be determined from the geochemical sampling. ERI was used to resolve bulk EC with depth along a survey line parallel to Lion Creek. The goal of the ERI was to investigate subsurface geologic structure along Lion Creek and to identify regions of elevated subsurface fluid EC with depth, which could not be done from EC logging in the stream. Additionally, a stilling well was installed to enable continuous measurement of stream stage, which was converted to discharge using a rating curve. The location of each data collection site is shown in Fig. 1. Precipitation and snow water equivalent (SWE) data from the Berthoud Summit Snowpack Telemetry (SNOTEL) site 8.2 km northwest of the field site (NRCS 2015) were used to investigate the response of the stream EC to rainfall and snowmelt. Details on all methods are described below.

Water Sampling

Water samples were collected in July and August at two sites for cations, trace metals, and total sulfur: Upper Lion Creek, at 50 m from the top of the study reach and Lower Lion Creek, at 440 m from the top of the study reach (Fig. 1). One 60 mL filtered (0.45 μm) aliquot of water was collected from the stream at each site. A new syringe, filter, and bottle were used for each aliquot. Filtration was done to minimize the particulates and colloidal materials in the samples. Each aliquot was acidified using trace metal grade nitric acid to pH <2 and stored at less than 4 °C until analysis. pH measurements were taken with a Thermo Scientific Orion 4-Star portable pH and fluid EC meter.

The samples were analyzed at the Colorado School of Mines (Golden, Colorado) for cations, trace metals, and total sulfur using inductively coupled plasma atomic emission spectroscopy (ICP-AES). In this study, sulfate concentrations were determined using the total sulfur measured with the ICP-AES, under the assumption that all sulfur was present as sulfate. Each ICP-AES run began with a blank, five standards, and two check standards to check the calibration. A check standard was run again after ten samples. A continuing calibration verification standard was used for the check standards.

The ratio of molar sulfate concentration to molar iron concentration can be used to determine how close to the AMD source respective waters are from because sulfate is more conservative than iron as it travels through the environment (e.g. Olías et al. 2004). Therefore, a lower sulfate to iron ratio indicates that AMD water is temporally or spatially closer to the AMD source (as long as no gypsum is present).

Streamflow

A stilling well was installed at the upstream end of the study reach (Fig. 1). The stilling well consisted of a 1 m long piece of PVC pipe with holes drilled in the side driven into the streambed and anchored with rebar on either side of the PVC. A HOBO water-level logger (Onset Computer Corporation, Bourne, MA) was placed inside the PVC and set to record pressure and temperature at 20 min intervals. An additional water level logger was placed on the

streambank to record barometric pressure. Water pressures in the stilling well were corrected for barometric pressure and converted to stream height.

Throughout the field season, six stream velocity profiles were measured just below the stilling well using the OTT MF Pro flow meter (OTT Hydromet, Kempten, Germany) and converted to stream discharge using the measured cross-sectional area of the stream. Measured stream discharge was plotted against the stream height, forming a rating curve. That curve was used to convert the stream heights measured at the stilling well to a continuous record of discharge. Velocities were measured when the stream was near its minimum and maximum height such that the rating curve was applicable for most flows during the study period.

Fluid Electrical Conductivity Logging

Three Solinst Levelogger 3001 probes were deployed 1 June 2015 along the stream reach: in Lower Lion Creek, at the 240 m seep, and at the 330 m seep (Fig. 1). The probes measure water pressure, temperature, and fluid EC. Point fluid EC and pH measurements were also taken by hand with a Thermo Scientific Orion 4-Star portable meter every 60 m along the study reach and at sampling sites throughout the field season. The pH and EC probes were calibrated prior to collecting field data, and were checked during field work. The measured fluid EC values were corrected to specific conductivity at 25 °C according to the method outlined in Radtke et al. (2005).

Concentration–Discharge Relationships

Relationships between individual constituent concentrations in a stream and discharge can be used to help understand the seasonal variation in constituent levels, predict constituent concentrations at various stream discharge levels (Malan et al. 2004), identify the source of a constituent in the stream (McDiffett et al. 1989), or to understand the underlying processes that control the concentration of the constituent (Godsey et al. 2009). A common mathematical form of the concentration-discharge relationship is:

$$C = aQ^b \tag{1}$$

where C is the constituent concentration (mg/L), Q is the stream discharge (L/s), and a and b are empirical constants (Hall 1970, 1971). In this case, a log–log plot of discharge and concentration is a straight line of zero slope (slope = $b = 0$) if the inflow concentration is chemostatic, or steady in time, meaning that the watershed system keeps the concentration of solutes constant, potentially as a result of attenuation processes in the stream, solubility controls on concentration, or inputs to the stream that have a similar concentration as the stream (Godsey et al. 2009). If the slope of the linear trend is −1, the relationship is perfectly dilution controlled.

Load of Total Dissolved Solids (TDS)

Measurements of stream EC are used here as a surrogate for the concentration of TDS in the AMD-impacted waters. TDS concentrations are in turn multiplied by estimates of stream discharge to determine TDS load. An empirical relationship between specific conductivity (SC), which is temperature corrected, and TDS concentration is given by Ebraheem et al. (1990):

$$log10(TDS) = 1.216 * log10(SC) - 0.584 \tag{2}$$

Equation 2 was applied successfully by Yuval and Oldenburg (1996) to data from an AMD site in Ontario, Canada, suggesting that the equation may be applied cautiously to other AMD sites.

Electrical Resistivity Imaging

Multiple ERI data sets were collected on a transect that roughly parallels Lion Creek at 2 week to 1 month intervals from 12 May to 2 October 2015. In all, 96 stainless steel electrodes were placed at 5 m intervals, making a 480 m long survey line. In this method, direct electrical current is transmitted through one pair of electrodes, called the transmitting dipole. The resulting potential is measured across a second pair of electrodes, called the receiving dipole. Each distinct electrode configuration is known as a quadripole. The ERI data were collected using a dipole–dipole sequence, which has an independent transmitting and receiving dipole and is sensitive to near-surface changes (Binley and Kemna 2005). Each survey included 1,829 quadripoles. A Syscal Pro resistivity meter (IRIS Instruments, Orleans, France) was used to collect the measurements. The location and elevation of each electrode was measured using a Trimble Geo7x GPS unit and post-corrected using a Pathfinder Office GPS.

Multiple measurements are taken at each quadripole to quantify noise; these repeated measurements are called a stack. Here, each quadripole measurement is the average of three to six stacked measurements, and a coefficient of variation was calculated at each quadripole for the stacked measurements. The electrical potential of a continuous medium as the result of a point source of current can be described by Poisson's equation (e.g. Binley and Kemna 2005; Day-Lewis et al. 2005; Loke et al. 2013; Rucker et al. 2009b):

$$-\nabla \cdot \sigma_b \nabla \phi = I\delta\left(x - x_s,\ y - y_s,\ z - z_s\right) \tag{3}$$

where σ_b is bulk EC (S/m), ϕ is electrical potential (V), I is electrical current (A), (x, y, z) is the position in space (m), (x_s, y_s, z_s) is the position of current source (m), ∇ is the

gradient operator, and δ is the delta function. This equation relates the electrical potential distribution in a medium to the bulk EC distribution. The field data collected using ERI consists of potentials and currents that can be translated to apparent conductivities, or the conductivity of an idealized homogeneous subsurface. An inverse method must be used to estimate a bulk EC model that explains the electrical potential data in the actual heterogeneous subsurface. Due to practical limitations on the amount and accuracy of data collected during an ERI survey, the inverse problem is inherently ill-posed, meaning many models may fit the field data with the same level of data misfit (Binley and Kemna 2005).

Our ERI inversions, or image reconstruction of bulk EC maps of the subsurface, were done using R2 version 2.7a, (Binley and Kemna 2005). This code uses an Occam's inversion scheme, which chooses the solution with a specified level of data misfit and the least complex structure; it is named after the heuristic technique Occam's Razor (deGroot-Hedlin 1990; LaBrecque 1996). A finite-element mesh was created to parameterize the inversion model using 1.25 m spacing in the x-direction along the stream, resulting in four boxes between adjacent electrodes. The mesh was spaced at 1 m intervals in the z-direction down to 10 m. Larger pixels were used at the edges to push the lateral and vertical boundary conditions away from the area of interest.

There are several ways to evaluate the inversion model results. In this study, the depth of investigation (DOI) index method of Oldenburg and Li (1999) was used to investigate how strongly the starting model affects the final bulk conductivity model. In the DOI method, the same data set is inverted using different homogeneous reference models. The resulting bulk EC models should be the same if they are independent of the reference model chosen. The DOI index is calculated for each cell in the final bulk EC model to determine how strongly the final model is affected by the reference model:

$$DOI(x,z) = \frac{1/\sigma_{b1}(x,z) - 1/\sigma_{b2}(x,z)}{1/\sigma_{b1r} - 1/\sigma_{b2r}} \quad (4)$$

where σ_{b1r} is the homogeneous bulk EC value from one reference model, σ_{b2r} is the bulk EC of the other reference model, and $\sigma_{bi}(x,z)$ is the bulk EC of the model cell at (x, z) using the inversion starting with the given bulk EC reference model. The DOI index should equal zero if the final bulk EC model is not affected by the reference model. The DOI index was calculated using a low reference model of 2 mS/m and a high reference model of 20 mS/m for each cell in the final bulk EC model, given a mean value of 10 mS/m from the data. The image transparency was increased for cells with DOI indices greater than 0.4 because the bulk EC of these cells is strongly influenced by the choice of reference model and is therefore less representative of the data.

Results and Discussion

Water Sampling

The ratio of sulfate to iron was calculated for the Upper and Lower Lion Creek samples; Upper Lion Creek consistently has a higher ratio of moles of sulfate per mole of iron, with ratios of 89:1, 284:1, and 391:1 for sampling dates 8 July, 4 August, and 14 August, respectively. Lower Lion Creek consistently has a ratio of 13:1 moles of sulfate to mole of iron for each sampling date. This result is consistent with influence from AMD in Lower Lion Creek but little influence from AMD in Upper Lion Creek.

The general geochemical composition of the collected water samples is detailed in Table 1. Aluminum, copper, iron, manganese, and zinc were all found in higher concentrations at the Lower Lion Creek sampling site compared to the Upper Lion Creek sampling site, suggesting the metals enter the stream in the study reach. There is a notable variation in cation concentrations with time at both the Upper and Lower Lion Creek sampling sites. Major cation concentrations generally increased from July to August at the Lower Lion Creek sample site, likely because the inputs from the seeps stayed fairly constant while the non-mine impacted input from snowmelt declined. This pattern is not so clear at Upper Lion Creek, where calcium and magnesium concentrations were constant, zinc increased, and aluminum decreased between these months.

Specific Conductivity and pH

Figure 2 shows the empirical inverse linear relationship between log10(SC) and pH measurements collected from Lion Creek and the seepage water. The trend between log10(SC) and pH is supported by many previous studies (e.g. Herbert 2006; Mighanetara et al. 2009); thus the specific conductivity measurements may be used to compare the extent of AMD contamination at different locations and times. There was more variation around the linear trend at higher pH values, which was possibly because the bicarbonate system buffers pH when the pH is around 6.1. The buffering system damps changes in pH but not in specific conductivity, resulting in a range of specific conductivity values for the same pH and subsequent departures from the linear trend. The seep and stream data both show high specific conductivity at low pH and follow the same linear relationship between specific conductivity and pH.

Table 1 Results of the geochemical analysis from samples collected in 2015 as well as calculated total dissolved solids (TDS) values at Lower Lion Creek

	8-Jul		4-Aug		14-Aug	
	Upper Lion Creek	Lower Lion Creek	Upper Lion Creek	Lower Lion Creek	Upper Lion Creek	Lower Lion Creek
S_T	2.67	68.7	3.64	95.1	3.69	105
Al_T	0.150	9.30	0.023	11.8	0.012	13.2
Ca_T	3.73	23.9	4.29	31.8	4.49	35.2
Cu_T	0.010	0.265	BDL	0.317	BDL	0.343
Fe_T	0.052	9.41	0.022	12.8	0.016	14.4
K_T	17.3	0.569	BDL	0.965	0.225	1.05
Mg_T	0.788	9.75	0.870	12.7	0.923	13.9
Mn_T	0.008	5.65	BDL	8.29	BDL	9.32
Na_T	3.33	4.67	3.73	5.50	3.79	5.82
SiO_2(aq)	7.79	15.5	7.97	18.0	8.04	19.1
Sr_T	BDL	0.089	BDL	0.112	BDL	0.122
Zn_T	0.027	0.32	0.10	0.47	0.12	0.57
pH	7.26	3.61	7.77	3.35	7.87	3.28
TDS (calculated)		317		473		542

Concentrations are in mg/L

BDL below detection limit

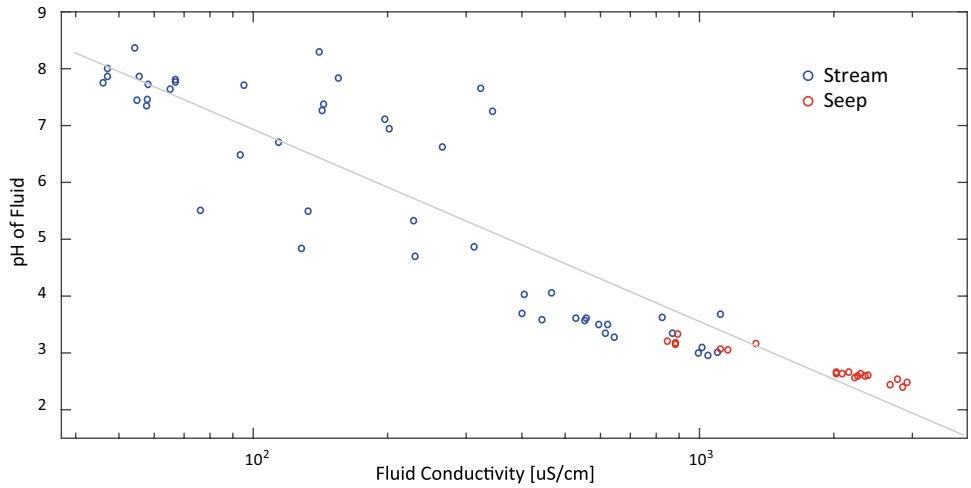

Fig. 2 pH versus the logarithm of specific conductivity. The trend line has the equation: $pH = -3.1 \times \log10(SC) + 13$; the trend has an R^2 value of 0.78 (p value <0.01)

Streamflow

Discharge declined rapidly from mid-June through mid-July, and then declined more slowly until the beginning of October, when there was a slight increase. Early season discharge follows the rapid decline in SWE values measured at the Berthoud Summit SNOTEL site (NRCS 2015), although the decline in SWE and the decline in discharge are offset by roughly 2 weeks (Fig. 3a). The offset is likely because SWE values measured at the Berthoud Summit SNOTEL site correspond to SWE on an exposed ridge that receives more solar radiation than the densely forested gulch that Lion Creek runs through. Heterogeneous snowmelt is common in forested watersheds such as Lion Creek (Boyer et al. 1997; Elder et al. 1991). Observations of snow along the study reach until the end of June indicate that there was snow in the watershed after SWE values dropped to zero at the SNOTEL site. The slower decline in stream discharge from mid-July to October was likely due to declining snowmelt inputs.

Stream discharge does not appear to be very sensitive to rainfall events when snowmelt is occurring, likely because summer rainfall primarily occurs as short duration, spatially variable thunderstorms. Therefore, we hypothesize that stream discharge is dominated by snowmelt in early summer and baseflow in later summer (Fig. 3a). In later summer, rainfall appeared to have a small impact on stream discharge; there was a slight increase in discharge at

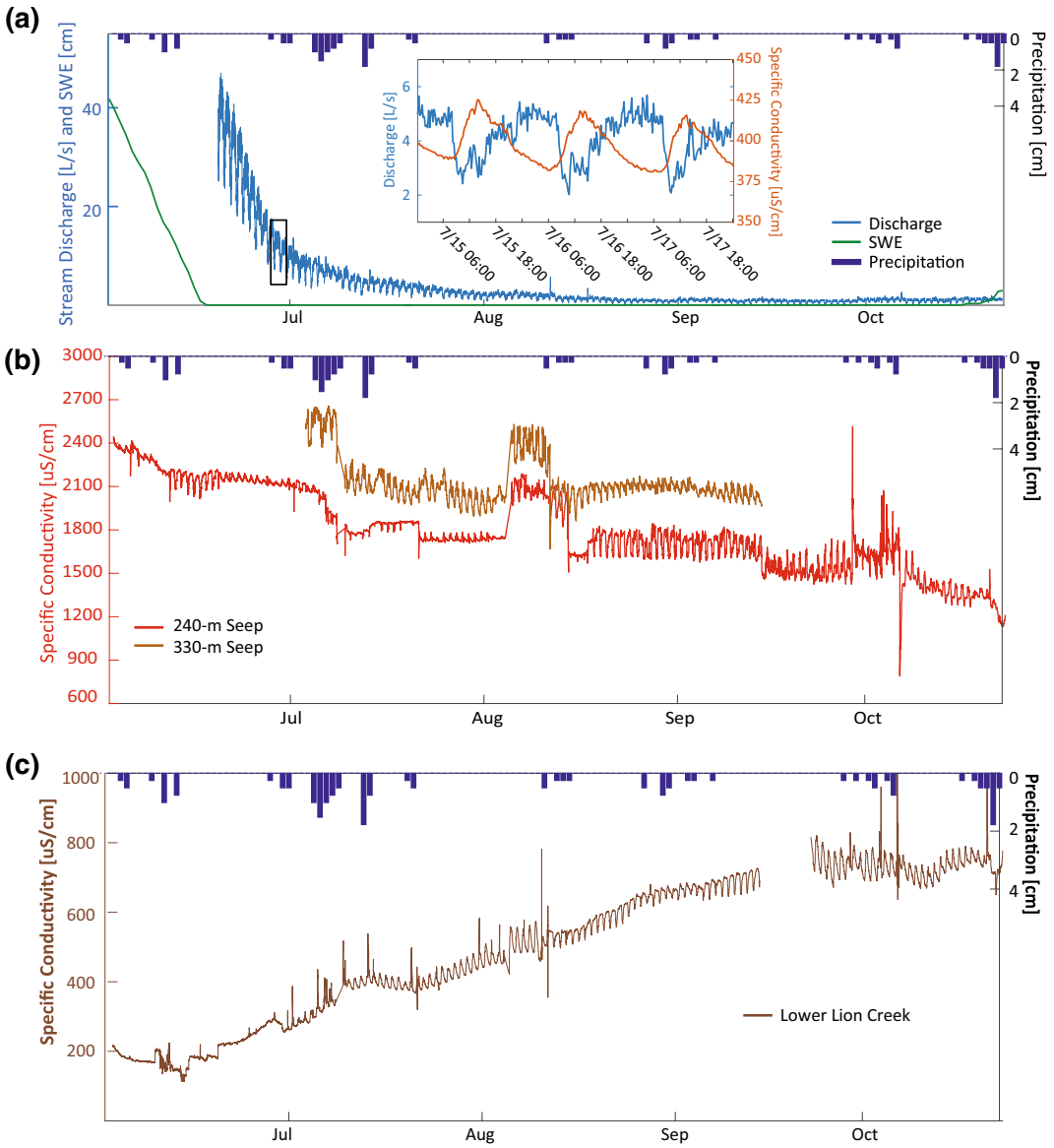

Fig. 3 **a** Lion Creek discharge, and snow water equivalent (SWE) depth and precipitation at the Berthoud Summit SNOTEL site. The *inset in the middle of the plot* shows discharge and Lower Lion Creek specific conductivity (SC) over two and a half days so that the diel cycle is apparent. **b** The time series of SC for the 240 and 330 m seeps and precipitation. **c** The time series of SC in Lion Creek and precipitation. Note the spikes in SC following some rainfall events

the beginning of October that corresponds with a cluster of rainfall events.

Stream discharge has a strong diel signal, with lower flow during the day and higher flow at night (Fig. 4). This is likely due in part to evapotranspiration removing water from the stream during the day and not at night and in part due to the timing of daily snowmelt. In June, discharge typically reaches its minimum value around 12:00 and then begins increasing (Fig. 4). Later in the season, discharge stays at its minimum value throughout the day and increases in the evening. This shift in the diel cycle is likely due to the input of snowmelt during the early part of the field season. The early afternoon increase in discharge seen during early summer is likely due to snowmelt from higher elevations reaching the stream gauge and continuing to contribute to the stream gauge through the night. The diel cycle shifts in late July such that discharge stays at a minimum throughout the day, as expected for a stream impacted by evapotranspiration during the daytime. At this time, snowmelt no longer contributes to the stream and evapotranspiration is the dominant process. The magnitude of the diel cycle decreases, and discharge stays at its daily minimum throughout the day.

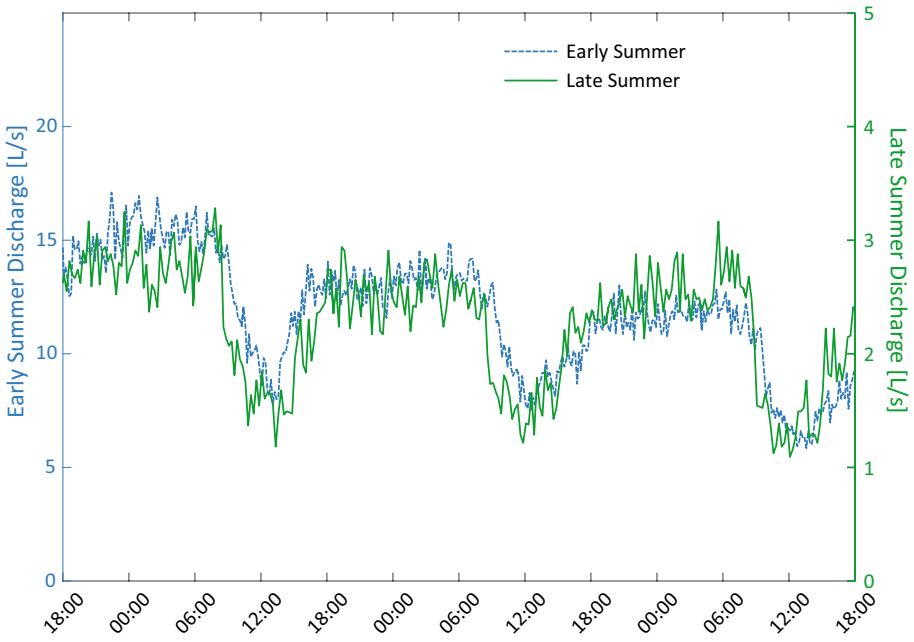

Fig. 4 Three days of stream discharge in early summer, 28 June 18:00–1 July 18:00, and late summer, 28 July 18:00–31 July 18:00. Note the difference in diel cycle between early and late summer

Fluid Electrical Conductivity Logging

We see seasonal, diel, and event-based changes in stream specific conductivity that reflect variations in TDS (Fig. 3c). Stream specific conductivity decreased during the first two weeks of June (Fig. 3c), likely because of large amounts of dilute snowmelt input based on a rapid decrease in SWE values during the same time period (Fig. 3a). Starting in the middle of June, stream specific conductivity began to increase, likely due to declining dilute snowmelt and rainfall input. In the third week of September, stream specific conductivity declined slightly due to a small increase in discharge related to rainfall events. Stream specific conductivity also has a strong diel signal, with higher specific conductivity during the day and lower specific conductivity at night (Fig. 3a, inset). This is likely due to changing amounts of dilution due to evapotranspiration and snowmelt, as indicated in the discharge diel cycle (Fig. 4).

The stream specific conductivity also increased in response to rainfall events. This is opposite of the dilution effect, but has been observed in numerous other studies and attributed to runoff washing metals deposited on the streambank by high flows back into the stream (e.g. Nordstrom 2011; Olías et al. 2004; Sarmiento et al. 2009). At this site, metal salts are visible on the streambank in the area where tailings are present, and in the large eroded area surrounding the 240 m seep. Rainfall runoff washing over these areas likely dissolved and mobilized these metals, causing the observed spikes in stream specific conductivity. In a study done in the Witwatersrand gold mining district of South Africa, Naicker et al. (2003) observed increasing soil-metal concentrations near the ground surface in an area that had never been covered by tailings. They attributed this phenomenon to high TDS groundwater being pulled into the unsaturated zone by capillary forces where it encountered surface evaporative demand. Some of the high TDS water evaporated, leaving behind metal salts. This same effect could also be occurring at this study site, causing metal salts to be deposited in the shallow subsurface along the stream, even spatially removed from the seeps and tailings pile. Thus, shallow groundwater paths containing metal salts could be activated during storms and contribute to the increase in specific conductivity related to rainfall.

The average daily stream specific conductivity increased by 250% between 3 June 2015 and 22 October 2015 (Fig. 3c). During this same time period, the average daily specific conductivity of seep water decreased by 50% (Fig. 3b), suggesting that different processes affected the concentration of dissolved species in the seep water than in the stream water over the study period. The decrease in seep specific conductivity followed the pattern reported by many first flush studies (e.g. August et al. 2002; Brooks et al. 2001), in which constituent concentrations increase during the rising limb of the stream hydrograph and decrease during the falling limb. Sullivan and Drever's (2001) study at Pennsylvania Mine, 20 km to the southwest of Minnesota Mine, showed a decline in mine drainage metal concentrations and an increase in stream metal concentrations from the time of maximum snowmelt to late summer baseflow, similar to the results in this study. This was likely because the elevated water table associated with early summer snowmelt inundated areas of the mine that were typically unsaturated the rest of the year. This flushed out accumulated weathering products, resulting in

higher TDS mine-drainage water during peak snowmelt. Stream specific conductivity showed the opposite seasonal response. Because the stream water was volumetrically dominated by snowmelt, and low TDS snowmelt dilutes TDS concentrations, stream specific conductivity was lowest during maximum snowmelt.

Here, the rainfall-runoff did not cause spikes in seep specific conductivity, in contrast to stream specific conductivity. In several instances in July, stream specific conductivity spiked upward as seep specific conductivity spiked downward (Fig. 3b). This suggests that in some instances, rainfall runoff diluted the concentration of dissolved constituents in the seeps along the stream, even as it washed more dissolved constituents into the stream.

Specific Conductivity-Discharge Relationships

The temporal resolution of the individual contaminant concentration data was too coarse to develop concentration–discharge relationships for each constituent. We therefore explored the relationship between stream specific conductivity and discharge (Fig. 5), although it is important to note that the discharge measurement is from the stilling well at Upper Lion Creek, while stream specific conductivity was measured at the Lower Lion Creek site (Fig. 1). While not explicitly highlighted in Fig. 5, the diel cycles in discharge and specific conductivity caused higher discharge and lower specific conductivity at night, meaning the data points shift downward and to the right from day to night. Many of the data points that fall above and to the right of the general linear trend are from days with rainfall as a result of the event-based increases in specific conductivity and slight increases in discharge due to rainfall.

The equation that best describes the data shown in Fig. 5 is

$$SC = 1585 * Q^{-0.32} \quad (5)$$

where SC is specific conductivity in µS/cm and Q is discharge in L/s. The exponent −0.32 in Eq. 5 indicates that the relationship between specific conductivity and discharge was between chemostatic (exponent of 0) and dilution (exponent of −1) (Godsey et al. 2009). We note that specific conductivity cannot determine chemostasis by constituent, as it only measures the composite ionic strength of the water. However, we suggest that the dilution portion of this system was due to the input of relatively clean water from snowmelt because the effect of rainfall is counter to the dilution effect, and stream discharge was not very sensitive to rainfall events (Fig. 3a). Additionally, input from groundwater not impacted by the mine, likely from upstream of the study reach, could have diluted the concentrations of AMD constituents.

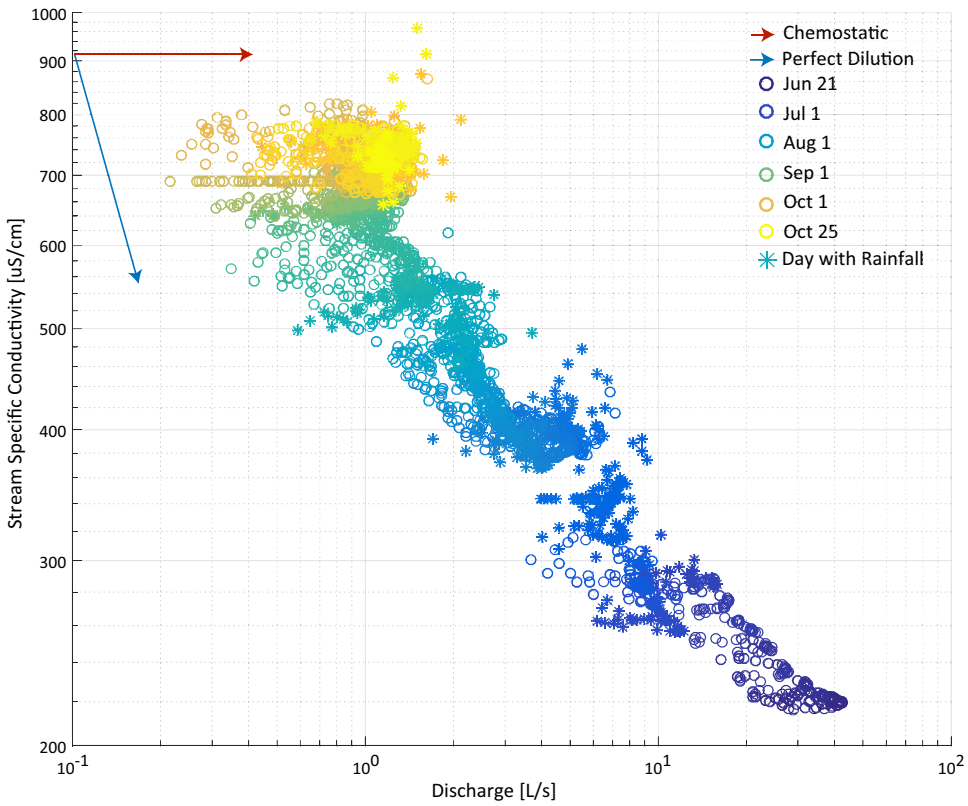

Fig. 5 Specific conductivity (SC) versus discharge from 19 June to 23 October 2015. The data points are hourly averages of SC and discharge data. *Asterisks* are used for data points on days in which precipitation occurred. The *blue arrow* indicates the pattern expected by perfect dilution, whereas the *red arrow* indicates a "chemostat", or more appropriately, constant fluid electrical conductivity data

Load of Total Dissolved Solids (TDS)

Stream TDS concentrations, calculated from the fluid EC logger at Lower Lion Creek, and stream discharge measured at Upper Lion Creek, were used to calculate a TDS load for the field season (Fig. 6). The spatial offset in the data sets certainly introduces some error into the calculated TDS load because additional water enters the stream along the reach between the Upper and Lower Lion Creek sites. However, over the field season, we found that the TDS load generally followed the same pattern as stream discharge. The load was highest in the early summer when stream TDS was low but discharge was high. The TDS load decreased to a minimum in September and then climbed slightly in October as stream specific conductivity increased slightly. It is important to note that much of the TDS load is made up of major elements that are not directly tied to AMD reactions. Byrne et al. (2017) calculated loading profiles along the stream for dissolved metals of concern during a single low flow day in August; this study presents continuous loading information for TDS from June to October 2015. We saw a strong diel signal in the TDS load throughout the field season. In early summer, this was due to the strong diel signal in discharge resulting from evapotranspiration occurring during the daytime and freshwater from snowmelt at higher elevations joining the stream. In late summer, the diel cycle of stream specific conductivity has a greater magnitude than that of stream discharge.

Electrical Resistivity Imaging

ERI data sets were collected along a fixed transect between May and October along the study reach. A single ERI image from 23 June is presented in Fig. 7 because the temporal trends in bulk electrical conductivity are small despite a strong seasonal trend in stream and seep specific conductivity. The raw, uninverted bulk EC data also did not show a significant change throughout the study period; the targets may be too small for detection with ERI. The average apparent bulk EC was between 7.4 and 8.0 mS/m for each data set through time. A one-way analysis of variance (ANOVA) test confirmed the hypothesis that the mean of each of the apparent bulk EC distributions was the same, to a confidence level of >99%.

The DOI index was calculated for each pixel in the inverted bulk EC model (Fig. 7). The 0.4 DOI contour is near or at the surface in the interval from 80 to 160 m along the study reach. In this transect section, it was difficult to minimize the contact resistance between the electrodes and the ground, resulting in larger stacking errors and measurements that were de-weighted in the inversion scheme. The model has a deep 0.4 DOI contour from 205 to 240 m along the study reach, indicating that current flowed deeper into the subsurface in that section, as a result of better contact between the electrodes and the ground as well as higher bulk EC close to the 240 m seep due to the highly mineralized soil water there.

The ERI map shows elevated bulk EC in the area of the 240 and 330 m seeps, but not in the vicinity of the 180 m seep. The difference here was likely because of the higher pH at 180 m, which appears to correlate with the

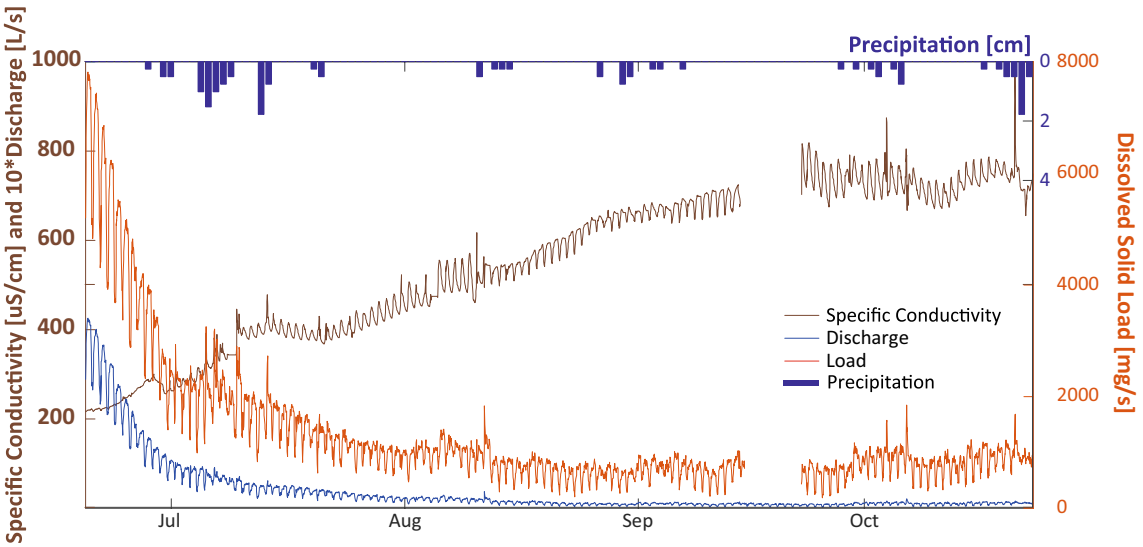

Fig. 6 Stream specific conductivity, discharge, total dissolved solids (TDS) load and precipitation from June to October. The TDS load is highest in early summer and shows large diel variation

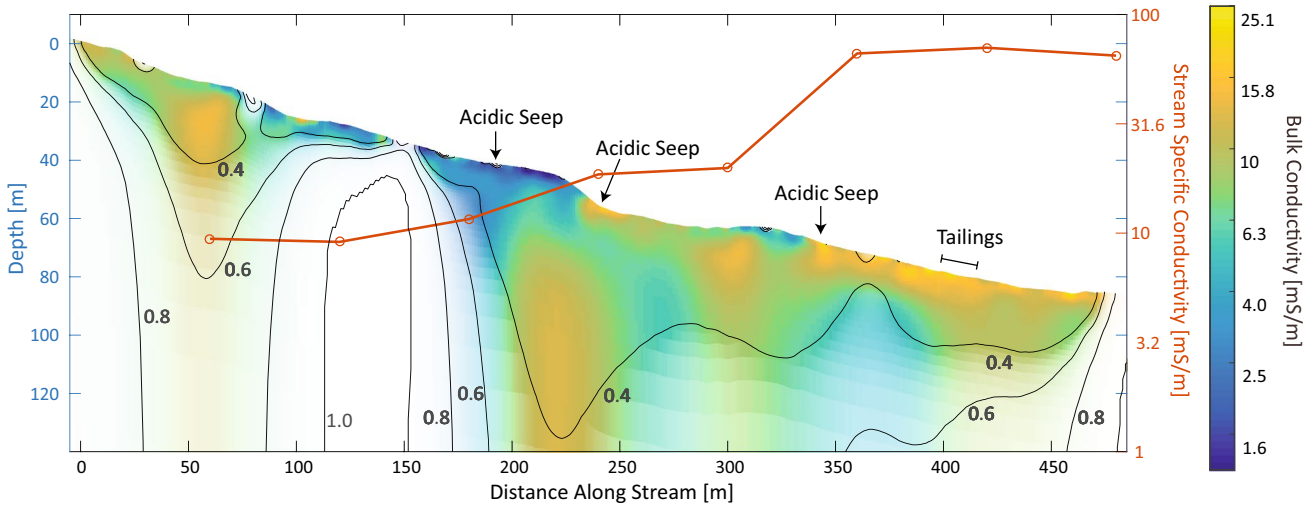

Fig. 7 Electrical resistivity imaging data set from 23 June 2015 with the average stream specific conductivity measured with the handheld probe in orange. The *black contour lines* indicate the depth of investigation index (DOI) index; parts of the inversion with a DOI index (Eq. 4) greater than 0.4 are increasingly transparent. Field observations of seeps and tailings are labeled

lower specific conductivity (Fig. 2) and thus a lower resultant bulk EC (Fig. 7). At about 315 m, the stream specific conductivity increased notably; at this location, the inversion shows a layer with low bulk EC at the surface underlain by a layer with higher bulk EC. We hypothesize that the conductive area in the subsurface from about 290 to 320 m along the study reach is a subsurface continuation of the 240 and 330 m seeps visible on the surface. The location coincides with the jump in specific conductivity of the stream (Fig. 7), so it is likely that the high specific conductivity, acidic water is mixing with the stream water over this section of the study reach. From about 360 m to the end of the study reach, the temporally averaged stream specific conductivity was nearly constant, suggesting that inputs to the stream in this section had a specific conductivity similar to that of the stream or were too small to affect in-stream specific conductivity.

The subsurface beneath the tailings piles from 390 to 410 m was more conductive than the area around it (Fig. 7). We hypothesize that when water infiltrates through the tailings, it leaches metals; this high specific conductivity water then infiltrated into the subsurface and caused the high bulk EC observed in the ERI image. There was no resultant increase in the temporally averaged stream specific conductivity adjacent to the tailings pile, however. This suggests that either there was no hydraulic connection between the subsurface beneath the tailings pile and the stream, or high TDS leachate enters the stream downstream from the study reach. Although the stream specific conductivity did not increase due to the tailings pile, if a hydraulic connection between the subsurface and the stream is established, high TDS leachate from the tailings pile could enter the stream as part of another diffuse source. The ERI data set itself cannot confirm this hypothesis, but it can be used to guide more invasive characterization efforts, such as drilling a well to physically access the subsurface.

There are two other notable high bulk EC areas visible in Fig. 7. One is located from about 40 to 55 m along the study reach. Another conductive area is located between 205 and 245 m along the study reach from about 60 m to the bottom of the ERI image. This latter anomaly is notable because the measurement sensitivity with depth is increased to about 80 m below the ground surface, indicating that the porous media conducted current to depths much greater here than elsewhere along the study reach. It is important to note that bulk EC is sensitive to lithology as well, so not every high bulk EC area is necessarily the result of acidic, high TDS AMD. The increase in bulk EC could be caused by higher permeability material, a conductive fracture, or higher clay content, for example; the actual cause can only be confirmed by drilling.

Conclusions

This study leveraged EC data in addition to geochemical analyses to investigate a headwater mountain stream affected by AMD. The objectives of our study were to identify diffuse and discrete contamination sources, to elucidate seasonal trends in water quality and loading, and to help inform ongoing remediation efforts. Measuring fluid and bulk EC is a low-cost method to determine the relative level of AMD contribution to a stream. The collection of bulk EC data in the shallow subsurface yielded information

about the spatial distribution of potential diffuse contamination entering the stream, and provides a guideline for future sampling locations. Additionally, fluid EC logging was valuable as a low-cost way to collect information about the general level of contamination in the stream and seeps throughout the field season. Although geochemical water samples yield more detailed water quality information and are important for understanding the chemical processes involved, it was impractical to get the same temporal resolution of water quality information using geochemical water samples alone.

Continuous discharge and stream specific conductivity data were collected from June to October, or from the falling limb of the stream hydrograph in early summer to late summer baseflow. Although stream specific conductivity increased during this period by 250%, seep specific conductivity decreased by 50%. Over the field season, seep specific conductivity declined from high first-flush levels and stream specific conductivity increased due to declining dilution from snowmelt, indicating that seasonal variation in stream specific conductivity was largely dilution controlled. The exception was following rainfall events, when there was an increase in specific conductivity as rainfall runoff dissolved soluble metal salts deposited on the streambank or in shallow groundwater flow paths that became saturated. The input of additional TDS from rainfall runoff is a source of diffuse contamination. TDS load, calculated using stream discharge and specific conductivity data, was highest during early summer, when discharge was highest. There was a large diel variation in the TDS load, likely due to the large diel fluctuation in stream discharge during the beginning of the field season and due to the diel cycle in specific conductivity toward the end of the field season. This information may be helpful for estimating the cost of different remediation scenarios, though more work is necessary to determine how much of the variation in TDS load was due to major ions versus metals.

Our results suggest that diffuse sources of AMD affect Lion Creek. First, the stream specific conductivity record shows spikes in specific conductivity during rainfall events, indicating that metal salts deposited on the streambank or shallow subsurface are washing into the stream with rainfall runoff. The tailings beside Lion Creek likely contributes to this effect. Second, there is visible iron precipitate on the streambed upstream from the identified discrete contamination entering the stream from the visible seepage faces. Finally, we identified a subsurface area where diffuse contamination was likely entering the stream. The ERI map shows areas of elevated bulk EC in the subsurface beneath the 240 and 330 m seeps as well as between the two seeps. The average stream specific conductivity showed a corresponding increase between the 240 and 330 m seeps. Because of this, we hypothesize that the two seeps have a subsurface portion as well that is contributing AMD-impacted water to the stream. However, bulk EC is sensitive to lithology as well as fluid EC; therefore, these data should be considered as a method of focusing new sampling in areas that might not have been previously considered, allowing for more spatially targeted remediation options. Our results lend themselves to a more invasive investigation of the 230–340 m section of the study reach. Drilling a well and analyzing water samples from the elevated bulk EC area identified by ERI (Fig. 5) could confirm that this area is indeed a source of diffuse contamination. Should this potential diffuse contamination source be confirmed, a prudent remediation option would be the installation of a permeable reactive barrier along the east bank of the stream from 230 to 340 m which could intercept discrete and diffuse contamination entering the stream in that reach.

Additionally, the ERI map shows a conductive area beneath the tailings pile at 390–410 m. This is likely due to acidic, high TDS leachate from the tailings infiltrating into the subsurface. Because there is not a resultant increase in stream TDS adjacent to the tailings pile, it appears that the tailings are not hydraulically connected with the stream. The tailings leachate is therefore a potential source of diffuse contamination; if the tailings are disturbed and the hydraulic connection with the stream is re-established, then high TDS leachate could enter the stream. This result suggests that removing the tailings beside Lion Creek is another remediation option, though care must be taken to avoid exposing more tailings to a weathering environment or establishing a more direct connection between the tailings and stream.

Acknowledgements A heartfelt thank you to all of the people who assisted with field work: Avery Becker, Zack Walter, and Curtis Weller, along with many others. In particular, AJ thanks Jackie Randell for lending her considerable expertise in each of the field methods employed in this study and for being a tireless field worker. We also thank Trez Skillern of the US Forest Service for providing access to the field site and the USGS Toxic Substances Hydrology Program for supporting Robert Runkel's time on this project. Finally, we thank Patrick Byrne, Katie Walton-Day, and two anonymous reviewers whose comments greatly improved this manuscript. Any use of trade, firm, or product names is for descriptive purposes only and does not imply endorsement by the US Government.

References

August EE, McKnight DM, Hrncir DC, Garhart KS (2002) Seasonal variability of metals transport through a wetland impacted by mine drainage in the Rocky Mountains. Environ Sci Technol 36:3779–3786

Banks VJ, Palumbo-Roe B (2010) Synoptic monitoring as an approach to discriminating between point and diffuse source contributions to zinc loads in mining impacted catchments. J Environ Monit 12:1684–1698

Banks D, Younger PL, Arnesen R-T, Iversen ER, Banks SB (1997) Mine-water chemistry: the good, the bad and the ugly. Environ Geol 32:157–174

Baresel C, Destouni G, Gren IM (2006) The influence of metal source uncertainty on cost-effective allocation of mine water pollution abatement in catchments. J Environ Manag 78:138–148

Baron JS, Campbell DH (1997) Nitrogen fluxes in a high elevation Rocky Mountain basin. Hydrol Process 11:783–799

Bencala KE, Walters RA (1983) Simulation of solute transport in a mountain pool-and-riffle stream: a transient storage model. Water Resour Res 19:718

Besser JM, Leib KJ (1999) Modeling frequency of occurrence of toxic concentrations of zinc and copper in the Upper Animas River. In: Morganwalp DW, Buxton HT (Eds), USGS Water-Resources Investigations Report 99 4018 A, pp 75–81

Bethune J, Randell J, Runkel RL, Singha K (2015) Non-invasive flow path characterization in a mining-impacted wetland. J Contam Hydrol 183:29–39

Binley A, Kemna A (2005) DC resistivity and induced polarization methods. In: Rubin Y, Hubbard SS (eds) Hydrogeophysics. Springer, Netherlands, pp 129–156

Boyer EW, Hornberger GM, Bencala KE, McKnight DM (1997) Response characteristics of DOC flushing in an alpine catchment. Hydrol Process 11:1635–1647

Braddock WA (1969) Geology of the Empire Quadrangle Grand, Gilpin, and Clear Creek Counties Colorado. USGS Professional Paper 616. https://pubs.er.usgs.gov/publication/pp616

Brooks PD, McKnight DM, Bencala KE (2001) Annual maxima in Zn concentrations during spring snowmelt in streams impacted by mine drainage. Environ Geol 40:1447–1454

Buselli G, Lu K (2001) Groundwater contamination monitoring with multichannel electrical and electromagnetic methods. J Appl Geophys 48:11–23

Butler BA, Ranville JF, Ross PE (2009) Spatial variations in the fate and transport of metals in a mining-influenced stream, North Fork Clear Creek, Colorado. Sci Total Environ 407:6223–6234

Byrne P, Reid I, Wood PJ (2013) Stormflow hydrochemistry of a river draining an abandoned metal mine: the Afon Twymyn, central Wales. Environ Monit Assess 185:2817–2832

Byrne P, Runkel RL, Walton-Day K (2017) Synoptic sampling and principal components analysis to identify sources of water and metals to an acid mine drainage stream **(in press Environmental Science and Pollution Research, Apr 2017)**

Caruso BS, Cox TJ, Runkel RL, Velleux ML, Bencala KE, Nordstrom DK, Julien PY, Butler BA, Alpers CN, Marion A, Smith KS (2008) Metals fate and transport modelling in streams and watersheds: state of the science and USEPA workshop review. Hydrol Process 22:4011–4021

Chandra AP, Gerson AR (2010) The mechanisms of pyrite oxidation and leaching: a fundamental perspective. Surf Sci Rep 65:293–315

Cunningham CG, Naeser CW, Marvin RF, Luedke RG, Wallace AR (1994) Ages of selected intrusive rocks and associated ore deposits in the Colorado mineral belt. USGS Bull 2109:1–37

Day-Lewis FD, Singha K, Binley AM (2005) Applying petrophysical models to radar travel time and electrical resistivity tomograms: resolution-dependent limitations. J Geophys Res B Solid Earth 110:1–17

deGroot-Hedlin C (1990) Occam's inversion to generate smooth, two-dimensional models from magnetotelluric data. Geophysics 55:1613

DeNicola DM, Stapleton MG (2002) Impact of acid mine drainage on benthic communities in streams: the relative roles of substratum vs. aqueous effects. Environ Pollut 119:303–315

Dodson MH (2004) Five-year review report for Clear Creek/Central City superfund site Gilpin and Clear Creek Counties. Colorado Health and Environment Hazardous Materials and Waste Division, Denver

Ebraheem AM, Hamburger MW, Bayless ER, Krothe NC (1990) Study of acid mine drainage using earth resistivity measurements. Ground Water 28:361–368

Elder K, Dozier J, Michaelsen J (1991) Snow accumulation and distribution in an Alpine Watershed. Water Resour Res 27:1541–1552

Evangelou VP, Zhang YL (1995) A review: pyrite oxidation mechanisms and acid mine drainage prevention. Crit Rev Environ Sci Technol 25:141–199

Godsey SE, Kirchner JW, Clow DW (2009) Concentration-discharge relationships reflect chemostatic characteristics of US catchments. Hydrol Process 23:1844–1864

Gozzard E, Mayes WM, Potter HAB, Jarvis AP (2011) Seasonal and spatial variation of diffuse (non-point) source zinc pollution in a historically metal mined river catchment, UK. Environ Pollut 159:3113–3122

Grayson RB, Gippel, CJ, Finlayson BL, Hart BT (1997) Catchment-wide impacts on water quality: the use of "snapshot" sampling during stable flow. J Hydrol 199:121–134

Hall FR (1970) Dissolved solids-discharge relationships: 1. Mixing models. Water Resour Res 6:845–850

Hall FR (1971) Dissolved solids-discharge relationships: 2. Applications to field data. Water Resour Res 7:591–601

Herbert RB (2006) Seasonal variations in the composition of mine drainage-contaminated groundwater in Dalarna, Sweden. J Geochemical Explor 90:197–214

Hornberger GM, Bencala KE, McKnight DM (1994) Hydrological controls on dissolved organic carbon during snowmelt in the Snake River near Montezuma, Colorado. Biogeochemistry 25:147–165

Johnson DB, Hallberg KB (2005) Acid mine drainage remediation options: a review. Sci Total Environ 338:3–14

Kimball BA, Runkel RL, Walton-Day K, Bencala KE (2002) Assessment of metal loads in watersheds affected by acid mine drainage by using tracer injection and synoptic sampling: Cement Creek, Colorado, USA. Appl Geochem 17:1183–1207

Kimball BA, Church SE, Besser JM (2006) Lessons learned from the U.S. Geological Survey abandoned mine lands initiative—1997–2002. In: Proceedings of 7th international conference on acid rock drainage (ICARD), pp 944–963

Kimball BA, Runkel RL, Walton-Day K (2010) An approach to quantify sources, seasonal change, and biogeochemical processes affecting metal loading in streams: facilitating decisions for remediation of mine drainage. Appl Geochemistry 25:728–740

Kleinmann RLP (1991) Acid mine drainage: an overview. In: Proceedings of Energy in the 90's. American Soc of Civil Engineers, Pittsburgh, PA, pp 281–286

LaBrecque DJ (1996) The effects of noise on Occam's inversion of resistivity tomography data. Geophysics 61:538

Loke MH, Chambers JE, Rucker DF, Kuras O, Wilkinson PB (2013) Recent developments in the direct-current geoelectrical imaging method. J Appl Geophys 95:135–156

Looby TB (1991) EPA superfund record of decision: Central City, Clear Creek. EPA ID: MOD006333975

Lovering TS, Goddard EN (1950) Geology and ore deposits of the Front Range, Colorado. USGS Professional Paper 223. https://pubs.er.usgs.gov/publication/pp223

Luther GW (1987) Pyrite oxidation and reduction: Molecular orbital theory considerations. Geochim Cosmochim Acta 51:3193–3199

Malan H, Bath A, Day J, Joubert A (2004) A simple flow-concentration modelling method for integrating water quality and water quantity in rivers. Water SA 29:305–312

Martín-Crespo T, Martín-Velázquez S, Gómez-Ortiz D, De Ignacio-San José C, Lillo-Ramos J (2011) A geochemical and

geophysical characterization of sulfide mine ponds at the Iberian Pyrite Belt (Spain). Water Air Soil Pollut 217:387–405
McDiffett WF, Beidler AW, Dominick TF, McCrea KD (1989) Nutrient concentration-stream discharge relationships during storm events in a first-order stream. Hydrobiologia 179:97–102
Mighanetara K, Braungardt CB, Rieuwerts JS, Azizi F (2009) Contaminant fluxes from point and diffuse sources from abandoned mines in the River Tamar catchment, UK. J Geochemical Explor 100:116–124
Moses C, Herman JS (1991) Pyrite oxidation at circumneutral pH. Geochim Cosmochim Acta 55:471–482
Moses CO, Nordstrom DK, Herman JS, Mills AL (1987) Aqueous pyrite oxidation by dissolved oxygen and by ferric iron. Geochim Cosmochim Acta 51:1561–1571
Naicker K, Cukrowska E, McCarthy TS (2003) Acid mine drainage arising from gold mining activity in Johannesburg, South Africa and environs. Environ Pollut 122:29–40
Nimick DA, Gammons CH, Parker SR (2011) Diel biogeochemical processes and their effect on the aqueous chemistry of streams: a review. Chem Geol 283:3–17
Niyogi DK, Lewis WMJ, McKnight DM (2002) Effects of stress from mine draiange on diversity, biomass, and function of primary producers in mountain streams. Ecosystems 5:554–567
Nordstrom DK (2009) Acid rock drainage and climate change. J Geochemical Explor 100:97–104
Nordstrom DK (2011) Hydrogeochemical processes governing the origin, transport and fate of major and trace elements from mine wastes and mineralized rock to surface waters. Appl. Geochemistry 26:1777–1791
NRCS (2015) Berthoud Summit SNOTEL Site 335. In: Nat Resour Conserv Serv SNOTEL Data. http://wcc.sc.egov.usda.gov/nwcc/site?sitenum=335. Accessed 20 Jan 2016
Oldenburg DW, Li Y (1999) Estimating depth of investigation in dc resistivity and IP surveys. Geophysics 64:403
Olías M, Nieto JM, Sarmiento AM, Cerón JC, Cánovas CR (2004) Seasonal water quality variations in a river affected by acid mine drainage: the Odiel River (South West Spain). Sci Total Environ 333:267–281
Radtke DB, Davis JV, Wilde FD (2005) Specific electrical conductance. US Geological Survey Techniques of Water Resources Investigations, book 9, chapt A6, sec 6.3, pp 1–22. http://pubs.water.usgs.gov/twri9A6/pp. Accessed 1 Feb 2016
Ramalho E, Carvalho J, Barbosa S, Monteiro Santos FA (2009) Using geophysical methods to characterize an abandoned uranium mining site, Portugal. J Appl Geophys 67:14–33
Rucker DF, Glaser DR, Osborne T, Maehl WC (2009a) Electrical resistivity characterization of a reclaimed gold Mine to delineate acid rock drainage pathways. Mine Water Environ 28:146–157
Rucker DF, Levitt MT, Greenwood WJ (2009b) Three-dimensional electrical resistivity model of a nuclear waste disposal site. J Appl Geophys 69:150–164
Runkel RL, Kimball BA, Walton-Day K, Verplanck PL, Broshears RE (2012) Evaluating remedial alternatives for an acid mine drainage stream: a model post audit. Environ Sci Technol 46:340–347
Runkel RL, Walton-Day K, Kimball BA, Verplanck PL, Nimick DA (2013) Estimating instream constituent loads using replicate synoptic sampling, Peru Creek, Colorado. J Hydrol 489:26–41
Runkel RL, Kimball BA, Nimick DA, Walton-Day K (2016) Effects of flow regime on metal concentrations and the attainment of water quality standards in a remediated stream reach, Butte, Montana. Environ Sci Technol 50:12641–12649
Sarmiento AM, Nieto JM, Olías M, Cánovas CR (2009) Hydrochemical characteristics and seasonal influence on the pollution by acid mine drainage in the Odiel river Basin (SW Spain). Appl Geochem 24:697–714
Sims L, Guerra J (2014) Updated fact sheet central city/clear creek superfund site. https://www.colorado.gov/pacific/sites/default/files/HM_sf-cccc-2014-factsheet.pdf. Accessed 15 Nov 2014
Sullivan AB, Drever JI (2001) Spatiotemporal variability in stream chemistry in a high-elevation catchment affected by mine drainage. J Hydrol 252:237–250
Taylor BE, Wheeler MC, Nordstrom DK (1984) Stable isotope geochemistry of acid mine drainage: experimental oxidation of pyrite. Geochim Cosmochim Acta 48:2669–2678
Walton-Day K, Runkel RL, Kimball BA (2012) Using spatially detailed water-quality data and solute-transport modeling to support total maximum daily load development. J Am Water Resour Assoc 48:949–969
Yuval D, Oldenburg DW (1996) DC resistivity and IP methods in acid mine drainage problems: results from the Copper Cliff mine tailings impoundments. J Appl Geophys 34:187–198